Research Square

Preprints are preliminary reports that have not undergone peer review.
They should not be considered conclusive, used to inform clinical practice,
or referenced by the media as validated information.

Ultrafast Mechanisms of Femtosecond Laser-Induced Structural Reconfiguration in Fluoride Glasses

Pengfei Wang

pfwang@nenu.edu.cn

Northeast Normal University

Liming Mao

Harbin Engineering University

Jiawei Wu

Institute of Semiconductors, Chinese Academy of Sciences https://orcid.org/0009-0002-6842-2413

Jiabao Du

Institute of Semiconductors, Chinese Academy of Sciences

Changhui Liu

Harbin Engineering University

She Lin

Harbin Engineering University

Shijie Jia

Harbin Engineering University

Shunbin Wang

Harbin Engineering University

Shusen Zhao

Institute of Semiconductors, Chinese Academy of Sciences https://orcid.org/0000-0002-8790-5261

Xuechun Lin

Institute of Semiconductors, Chinese Academy of Sciences https://orcid.org/0000-0002-6376-0846

Yichun Liu

Northeast Normal University https://orcid.org/0000-0002-8628-6112

Article

Keywords:

Posted Date: December 22nd, 2025

DOI: https://doi.org/10.21203/rs.3.rs-8213333/v1

License: This work is licensed under a Creative Commons Attribution 4.0 International License.
Read Full License

Additional Declarations: There is **NO** Competing Interest.

Version of Record: A version of this preprint was published at Nature Communications on September 9th, 2026. See the published version at https://doi.org/10.1038/s41467-026-77719-2.

Abstract

Femtosecond laser direct writing enables precise three-dimensional structuring of transparent materials, yet the underlying modification mechanisms in fluoride glasses—key platforms for mid-infrared photonics—remain elusive. Here, we elucidate the ultrafast-to-microscale mechanisms governing femtosecond laser-induced modification in fluoroindate glass by integrating time-resolved pump–probe shadowgraphy, birefringence imaging, and microscopic elemental analysis. Plasma evolution dynamics reveal peak electron densities approaching 5×10^{20} cm^{-3} at 1.2 ps, accompanied by gigapascal-level stress waves propagating at ~ 4.3 μm/ns. These transient processes generate steep thermal–pressure gradients that drive selective migration of heavy and light ions, producing polarizability-dependent refractive index changes ($\Delta n \approx 10^{-3}$–10^{-2}). By correlating plasma dynamics, stress evolution, and compositional redistribution, we establish a unified framework linking energy deposition and structural reconfiguration. The results clarify that positive index regions originate from cation densification (Pb/In enrichment), whereas negative regions arise from anion expansion (F/Ba migration). This mechanistic insight provides general design principles for controllable femtosecond-laser processing of fluoride glasses and extends to the rational engineering of low-loss, mid-infrared integrated photonic components.

Introduction

Fluoride glasses—represented by fluorozirconate and fluoroaluminate systems—offer irreplaceable advantages for mid-infrared (MIR) applications[1–3]. Their unique combination of low phonon energy (~ 500–600 cm^{-1}), broad transmission window (0.2–8 μm, spanning ultraviolet to MIR), and excellent rare-earth ion solubility enables MIR lasers, gas sensors, and high-precision optical systems with unparalleled performance[4–7]. For instance, Er^{3+}-doped fluoride fibers achieve significantly enhanced laser efficiency at 3.5 μm[8], a wavelength critical for trace gas detection of pollutants like volatile organic compounds. However, the practical implementation of fluoride glasses in photonic integrated circuits (e.g., for miniaturized, high-throughput photonics) has long been constrained by the lack of precise, scalable microstructure engineering techniques.

Femtosecond laser direct writing has emerged as a revolutionary tool for three-dimensional micro-nano processing of transparent materials, owing to its non-thermal processing nature and sub-micrometer spatial resolution[9,10]. Unlike continuous-wave or nanosecond lasers, which induce large heat-affected zones (leading to crystallization or phase separation in fluoride glasses), femtosecond pulses deposit energy via nonlinear ionization (multiphoton and avalanche ionization) on a timescale shorter than lattice thermalization (100 fs–1 ps), enabling ‘cold’ material modification[11]. This ultrafast laser-based writing capability has been applied to fabricate waveguide cores for photonic integrated circuits in silicate and germanate glasses[12,13]. However, fluoride glasses present unique challenges: their ionic bonding, low mechanical strength (elastic modulus ~ 50–60 GPa, ~ 70% of silicates), and high sensitivity to laser-induced defects result in complex, poorly understood modification phenomena[14,15]. For

example, femtosecond laser-written waveguides in fluorozirconate glasses exhibit positive refractive index changes exceeding 2×10^{-2}, yet the mechanistic link between laser-matter interactions and such refractive index modulation remains elusive[16]. This knowledge gap severely hinders the rational design of high-performance fluoride glass waveguides for next-generation photonic devices.

Laser-matter interactions between ultrafast lasers and transparent materials are well established for oxide glasses (e.g., fused silica)[17]. Studies show the modification process initiates on the femtosecond timescale: intense laser fields drive nonlinear photoionization of the wide-bandgap material, generating a transient dense plasma (electron density: 10^{19}–10^{21} cm^{-3})[18,19]. Next, on the sub-nanosecond to nanosecond timescale, fluid dynamic relaxation occurs—including shockwave/stress wave emission and thermal diffusion—where relaxation of the laser-heated volume triggers elastic/plastic stress waves, leading to permanent structural rearrangements (e.g., densification or cavity formation)[20,21]. On the microsecond timescale, thermal energy fully diffuses out of the focal region, ultimately manifesting as material modifications (e.g., altered density, coordination environment, or lattice defects) that directly induce refractive index modulation[22,23]. Despite this progress, femtosecond laser modification mechanisms in fluoride glasses remain underexplored. The weak ionic bonding in fluoride glasses lowers ionization thresholds; however, correlations between plasma characteristics (e.g., peak electron density, temporal evolution) and femtosecond pulse parameters remain unestablished. Additionally, fluoride glasses exhibit lower shear moduli (≈ 15–25 GPa) and higher thermal expansion coefficients (≈ $15–25\times10^{-6}$ K^{-1}), which alter stress wave propagation and relaxation[14,24]. Existing work on femtosecond lasers in fluoride glasses focuses primarily on waveguide fabrication and performance (e.g., propagation loss, mode profile)[25–29], with insufficient study of transient physical processes—preventing the establishment of a link between ‘microscale modification’ and ‘macroscopic Δn’.

In this work, we investigate femtosecond laser-induced modifications in fluoride glasses across multiple time scales, linking these insights to the phenomena and key characteristics of femtosecond laser-written optical waveguides. Using femtosecond time-resolved pump-probe shadowgraphy and an improved birefringence imaging system, we characterized the spatiotemporal dynamics of plasma and stress waves generated in fluoroindate glass. Microscale analyses of waveguide regions included electron probe microanalysis of elemental migration and advanced phase imaging of refractive index distributions. Additionally, we demonstrate thermal erasure and structural transformation of channel waveguides. We systematically elucidate the mechanism underlying femtosecond laser-induced modification of fluoride glasses, providing a reliable framework for designing femtosecond laser-written fluoride waveguides with controllable refractive index contrast. This work will advance the development of mid-infrared optoelectronic integrated circuits.

Results

Femtosecond laser time-resolved pump-probe shadowgraphy

The essence of ultrafast laser-induced material modification is governed by exciton-electron interactions and subsequent transient physical changes[30,31]. Characterizing the evolution of plasma and stress waves thus provides critical insights into laser-material interaction dynamics. As shown in Figs. 1a and 1b (see "Materials and Methods" for details), femtosecond time-resolved pump-probe shadowgraphy and an improved birefringence imaging technique were used to detect the generation and evolution of plasma and stress waves, respectively. Notably, the time delay between the probe and pump beams was adjusted by the 'delay line' in the probe optical path. After frequency-doubling the 1040 nm femtosecond laser, a linear polarizer and quarter-wave plate were added, and the CCD was replaced with a polarization camera to record the anisotropic optical responses (birefringence) of the laser-irradiated sample (Fig. 1b). Additionally, the detection directions for plasma and stress waves were oriented vertically and horizontally, respectively, relative to the pump beam direction.

Fluoride glasses are primary materials for MIR research, offering key advantages of low phonon energy and broad transmission windows. Mature fluoride glass systems include fluorozirconate (ZrF_4-based/ZBLAN)[1], fluoroaluminate (AlF_3-based/ABYPM)[32], fluoroindate (InF_3-based/INF)[33], and a novel fluorozincate glass (ZnF_2-based/AZF)[34]—modified from fluoroaluminate compositions. Among these, fluoroindate glasses exhibit the lowest phonon energy (~510 cm^{-1}) and the broadest transmission window (0.2–10 μm)[35]. Thus, we used home-made fluoroindate glass as our primary research material (see 'Materials and Methods' for INF glass synthesis). Fig. 1c shows the transmittance spectrum of INF glass: compared to chalcogenide glasses (which have longer transmission windows), INF glass achieves higher transmittance (>90%) over 0.2–7 μm, whereas chalcogenide glasses only reach ~50–70% transmittance in this range[36]. This broadband high-transmittance property is irreplaceable. The intrinsic refractive index of the glass is critical for simulating and calculating transient physical processes. As shown in Fig. 1d, the refractive indices of INF glass are 1.542 at the probe beam wavelength (520 nm) and 1.526 at the pump beam wavelength (1040 nm). Fig. 1e presents the differential thermal analysis curve of INF glass, with a glass transition temperature (T_g) of ~250°C and crystallization temperature (T_x) of ~349°C, yielding a ΔT of 99°C—indicating excellent fiber-drawing capability.

Transient temporal-spatial evolutions of plasma

Plasma-lattice interactions in glass are the direct driver of structural modifications. Femtosecond laser-induced nonlinear ionization in transparent materials generates electron plasma, primarily involving multiphoton ionization and avalanche ionization for pulse durations on the hundreds-of-femtosecond timescale[30,37,38]. When the instantaneous power exceeds the modification threshold, plasma becomes observable via imaging. By adjusting the single-pulse energy of the femtosecond laser focused inside the glass, we captured weak plasma generation in INF glass at 0.16 μJ (Fig. 2a). This single-pulse energy corresponds to a power density of ~1.19×10^{13} W cm^{-2}, with the modified region length reaching ~9 μm. As the power increased to 2.81 μJ, the modified region length extended to 60 μm, and the nonlinear focal position shifted progressively forward. This behavior arises because, in transparent media with positive nonlinear refractive indices, laser pulses with power exceeding the self-focusing critical power undergo

contraction along the propagation axis—leading to a significant focal length reduction with increasing laser intensity[39].

To quantify carrier density from optical measurements, we combined the Beer–Lambert law (for free-carrier absorption coefficient calculation) with the Drude model to compute electron density (See details of the calculation in Supplementary Note 1). We recorded time-resolved plasma images at a pulse energy of 5 μJ, alongside reference images (without pump laser irradiation; Fig. 2b). Subsequent denoising of the time-resolved plasma images and extraction of transmittance information yielded the final plasma images. Higher pulse energies expanded the originally 'filamentous' modified region into an inverted 'droplet' shape, which corresponds to the true spatial extent of the femtosecond laser focal region.

Femtosecond laser-induced transient phenomena differ significantly across glass materials, which inherently reflect variations in the dynamic efficiency of the 'laser energy absorption' to 'free electron generation' process. We performed femtosecond laser plasma experiments on the four aforementioned fluoride glass substrates and quantified the dependence of electron density on single-pulse energy and delay time (Figs. 2c, d). The femtosecond laser single-pulse energy was varied from 0.4 to 5 μJ. Saturation electron densities were achieved at 0.8 μJ (INF), 1 μJ (ABYPM), 2 μJ (AZF), and 2.5 μJ (AZFD), corresponding to electron densities of 4.73×10^{20}, 4.77×10^{20}, 4.11×10^{20}, and 4.39×10^{20} cm^{-3}, respectively. Compared to fused silica—where plasma electron density reaches 1.29×10^{20} cm^{-3} at 12 μJ (ref. 17)—fluoride glasses exhibit lower saturation thresholds and higher electron densities. This directly confirms that fluoride glasses have smaller bandgap energies and larger multiphoton absorption cross sections, particularly INF and ABYPM. At saturation threshold, the delay times for peak electron density differ slightly across glasses: ABYPM and AZF reach peaks at 800 fs, while INF and AZFD peak at 1200 fs. These differences arise from factors including the 'initiation competition' of the ionization process, electron energy dissipation, and defect states. For instance, within the same fluoride glass system, variations in network structure (e.g., F^- ion distribution, cation vacancies) create distinct defect states that bidirectionally modulate electron density growth kinetics—either by promoting seed electron generation or trapping free electrons. Notably, introducing trivalent cations (e.g., GaF_3 in InF_3-based glasses) enhances fluoride glass network stability[40,41]. Compared to AZFD (with Dy^{3+} doping), the AZF system contains more cation vacancies, leading to additional defect energy levels. These defects reduce the effective bandgap for multiphoton ionization, thereby shortening the electron density peak delay time.

Once the pump energy reaches the material damage threshold, the maximum electron density plateaus. We present time-resolved plasma images and corresponding electron density evolution of INF glass at saturated electron density (0.8 μJ), recorded over 400 fs–5 ps (Figs. 3a, b). The pump beam is incident along the Z-direction, with the leftmost edge of the image 115 μm from the glass surface. At 400 fs, distinct plasma is observed, with a length of ~16 μm. Notably, the femtosecond laser pulse duration was 400 fs, so the time delay interval was set to 400 fs; however, plasma formation onset occurred earlier in

practice. As the time delay increases, the plasma profile evolves slightly differently in the transverse (perpendicular to the laser incidence direction) and longitudinal directions—details more clearly resolved in electron density images. For a single pulse, the maximum transverse profile (~2.1 μm) is achieved at 800 fs, comparable to the theoretical femtosecond laser spot size in INF glass. The longitudinal profile peaks at ~27.7 μm at 2.8 ps, then gradually decreases. This indicates that the femtosecond laser modification profile in transparent materials is primarily determined by the pump beam waist diameter and incidence direction.

Figs. 3c and d show the spatial distribution of transient electron density along the plasma axis and the spatiotemporal evolution of peak electron density over 400 fs–5 ps. Throughout the delay range, the transient peak electron density remains almost near the nonlinear focal point. Minor positional shifts of the peak density within the focal region at specific delays may correlate with ionization concentration in the plasma formation zone. The transient electron density first rapidly increases, peaking at 1.2 ps (4.73×10^{20} cm^{-3}), then decays gradually with increasing time delay—consistent with the temporal profile of the pump pulse intensity. This transient plasma serves as the core energy carrier linking laser irradiation and stress wave generation. Specifically, the plasma accumulates energy via free-carrier absorption, transfers it to the lattice through electron–phonon coupling, and induces localized rapid heating. Temperature-driven lattice thermal expansion is constrained by the surrounding glass matrix generating thermoelastic pressure that follows the scaling relation where the pressure change (Δp) is proportional to the peak electron density ($n_{e,peak}$) and laser fluence (F). This pressure propagates through the glass as acoustic waves, forming stress waves. Thus, the energy dissipated by the plasma serves as the "energy source" for stress waves, with the total dissipated energy determined by the electron density and laser fluence.

Stress wave detection based on birefringence imaging

The interaction between femtosecond lasers and dielectric materials exhibits distinct processes across different characteristic time scales. For example, energy deposition on the hundred-femtosecond scale and mechanical material responses on the tens-of-picosecond scale have been reported[19]. The efficiency of energy transfer from electrons to the lattice is governed by the free electron concentration: higher electron densities enhance electron–phonon collision frequencies, thereby accelerating the conversion of electronic kinetic energy into lattice thermal energy. This energy-driven lattice heating induces thermal expansion, generating a pressure field whose magnitude scales positively with the peak electron density. As this pressure field propagates elastically through the glass matrix, it manifests as observable stress waves.

We modified the plasma detection optical path (Fig. 1b) and employed a polarization camera at the detection end to record the optical responses of fluoride glasses under femtosecond laser irradiation (see details in Supplementary Note 2). From the optical transmission images (Fig. 4a), we observed a rapid transmittance decrease in the laser-irradiated focal region, attributed to free-carrier absorption during photoionization. Subsequently, on the picosecond time scale, local transmittance increased in the

focal region (most pronounced at 100 ps), indicating free-electron recombination. Fig. 4b shows corresponding optical retardance images, which enable more precise analysis of stress wave propagation than transmission images. At 100 ps, optical retardance intensity increased significantly, followed by outward propagation at 200–300 ps. On the nanosecond time scale, stress waves propagated distinctively away from the focal region, spreading radially outward from the focal point. The stress wave propagation speed was ~4.3 μm/ns, which can serve as a reference for the sound velocity in fluoride glasses.

Optical retardance can be used to estimate laser-induced internal stress in materials. The stress-optic law states that the principal stress difference ($\Delta\sigma$) and optical retardance (δ) are linearly correlated via $\Delta\sigma = (\delta\lambda)/(2\pi hC)$, where h is the stress wave propagation path length and C is the stress-optic coefficient[42]. For INF glass at the probe wavelength (520 nm), pressure testing determined $C=0.55 \times 10^{-12}$ $N^{-1}m^2$. Fig. 4c shows the time-dependent evolution of the stress difference between the center and periphery of the stress wave. At 0.8 μJ, the generated stress reaches gigapascal levels, with maximum values of ~1.47 GPa at the focal center (100 ps) and ~1.23 GPa at the periphery (800 ps). Based on the relationship between thermal stress and temperature change[43], the focal center and stress wave periphery correspond to local temperature rises of ~1500 K and ~1250 K, respectively. For stress evolution, a large population of excited free electrons recombines on an ultrafast timescale, transferring most of their energy to the lattice and thus inducing an instantaneous stress surge in the central region. As time evolves (0 to 0.8 ns), the central stress gradually propagates outward to the periphery, leading to a decrease in central stress and a concomitant increase in peripheral stress. Beyond 0.8 ns, ongoing free-electron recombination sustains energy transfer to the lattice, manifesting as a subsequent rise in central stress. The birefringence distribution (Fig. 4d) reveals that stress arising from transient lattice expansion in the laser-irradiated central excitation region propagates radially, with a predominant orientation along a specific direction (double-arrowed direction). Furthermore, we assessed the contribution of electronic effects to stress wave generation by estimating the electron pressure P_e at saturated electron density using the relation $P_e = n_e k_B T_e$, where k_B is the Boltzmann constant and T_e denotes the average electron temperature (set to 5 eV)[19]. This calculation yields an electron pressure of ~0.38 GPa, which is substantially smaller than the experimentally measured stress amplitude (~1.23-1.47 GPa). These results confirm that stress wave generation is dominated by lattice thermal expansion, which is driven by energy transfer from the electronic subsystem to the lattice, rather than direct impact from the electron plasma.

Microscale analysis of femtosecond laser-modified regions

Femtosecond laser irradiation induces distinct modifications in transparent glasses, including permanent damage and refractive index gradients. Characterizing the optical and material properties of modified microregions provides insights into the underlying modification mechanisms—critical for femtosecond laser direct writing of optical waveguides, where refractive index characterization directly dictates waveguide fabrication strategies and optimal device dimensions. We measured the refractive

index distribution of femtosecond laser-modified INF glass cross-sections using the method from ref. 44 (Fig. 5), which combines a modified near-field approach and quantitative phase imaging to map 2D refractive index profiles of complex direct-written waveguide structures.

Fig. 5a shows micrographs of single-line modified regions: at a 1 kHz repetition rate, the modified zone exhibits a filamentous profile along the laser incidence direction, elongating with increasing single-pulse energy. Refractive index maps reveal that negative index changes dominate the modified region, with a contrast of 10^{-2} (ranging from -6×10^{-3} to 4×10^{-3})—consistent with previous reports that low repetition rates produce small refractive index reduction traces. We fabricated channel waveguides (see ref. 45 for writing protocols) with a lateral width of ~10 μm, matching typical fiber core dimensions (see Fig. 5b). As single-pulse energy increases, the negative-index modified region elongates longitudinally until it reaches the boundary of the positive-index region. Glasses with low melting points and high thermal expansion coefficients typically exhibit reduced refractive index under femtosecond laser-induced thermal shock[22,46], arising from volume expansion and material rarefaction—supported by Raman spectroscopy (see details of the Raman characterization in Supplementary Note 3). Additionally, multi-scan writing uniformly extends the variation of the single-line refractive index along the transverse direction, with a distinct positive-index modification zone appearing at the pulse front ($\Delta n \approx 5 \times 10^{-3}$).

We further used electron probe microanalysis to characterize elemental redistribution in the cross-section of femtosecond laser-modified INF glass. Fig. 6 presents backscattered electron (BSE) image and corresponding elemental distribution maps. Cross-sectional BSE image reveal that the modified zone forms an inverted droplet shape under a 50 kHz repetition rate and 500 μm/s scanning speed (100 pulses per position), with the femtosecond laser incident along the Z-direction. Compared to filamentous modification traces observed under low repetition rates or single-pulse excitation, high repetition rates and relatively larger single-pulse energies induce expanded regions far exceeding the laser spot waist diameter[29,47]. BSE images of the modified region exhibit distinct brightness contrast, corresponding to positive/negative relative refractive index changes.

We also provide wavelength dispersive spectrometer (WDS) mapping results for the region (Li was undetectable due to its low energy). These maps reveal a competitive mechanism of thermal gradient-driven diffusion and charge-compensated migration governing elemental redistribution. Heavy metal cations (Pb^{2+}, In^{3+}) are enriched in the central high-pressure region, consistent with their tendency to accumulate in zones of compressive stress induced by stress wave convergence. Light anions (F^-) and Ba^{2+} are pushed toward the peripheral regions, likely driven by outward thermal diffusion from the high-temperature core. The primary glass components (In^{3+} and F^-) exhibit analogous enrichment behaviors to Pb^{2+} and Ba^{2+}, respectively, albeit with more subtle changes, reflecting a coordinated migration to maintain local charge neutrality. To confirm the universality of this mechanism, we conducted WDS testing on the femtosecond-modified region of ABYPM glass (see details in Supplementary Note 4), where Pb^{2+}, F^-, and Ba^{2+} showed identical migration patterns to those in INF glass. This consistent elemental partitioning directly stems from the competition between pressure-driven cation aggregation

and thermal gradient-induced anion expulsion, ultimately leading to significant local polarizability differences. Such polarizability variations, coupled with the compositional inhomogeneity, account for the observed sign inversion of refractive index change (Δn) across the modified zone. Significant elemental migration was also observed in fluorozirconate glasses[16], indicating that positive refractive index changes primarily stem from densification caused by enrichment of Ba, Ce, Yb, and Er in positive index contrast regions. Collectively, these elemental distribution results demonstrate that refractive index changes in femtosecond laser-modified regions arise from polarizability differences induced by elemental migration.

Femtosecond laser direct-writing channel optical waveguide

The femtosecond laser writing strategy for optical waveguides depends on the response of dielectric materials to laser irradiation. For instance, distinct waveguide structures (Type I/II/III) are fabricated based on refractive index distribution differences in modified regions, ensuring light propagation is confined to high-refractive-index domains[13]. At low repetition rates, low-refractive-index regions dominate the modified structure of fluoride glasses (50–80% proportion), consistent with previous observations in fluorozirconate glasses[48]. We fabricated channel waveguides in INF glass via multi-scan writing (260 μm from the glass surface) at a fixed repetition rate of 1 kHz and writing speed of 500 μm/s. Fig. 7a shows channel waveguide images fabricated with single-pulse energies of 0.3 and 0.4 μJ. Three writing intervals (0.5, 0.8, 1.0 μm) were tested at each energy, with waveguide width controlled to 10 μm via scan number adjustment. Cross-sectional waveguide images exhibit uniform brightness variations (corresponding to refractive index increases/decreases), with the bright area proportion increasing slightly with larger writing intervals. End-face coupling measurements yielded a minimum waveguide insertion loss of ~0.7 dB/cm.

Heat-treatment was performed on INF glass samples containing waveguides to verify the thermal stability of femtosecond laser-written micro/nanostructures (Fig. 7b). Results show that under constant heat treatment duration, the modified regions gradually erased as temperature increased (up to near the glass transition temperature), with more pronounced erasure for lower writing energies (See additional thermal erasure comparisons in Supplementary Note 5). Additionally, waveguides written with higher single-pulse energies may develop significant cracks, which are thermally irreversible. These permanent defects substantially increase waveguide transmission loss. During waveguide fabrication, we observed that refractive index-modified regions can be transformed into one another by simply adjusting the writing depth (Fig. 7c). Vertical translation and repetitive writing on pre-existing waveguides enable mutual conversion of positive/negative refractive index regions and expansion of positive-index regions —providing a new strategy for waveguide structural design.

Discussion

Femtosecond laser irradiation of fluoride glasses triggers spatiotemporal processes spanning femtoseconds to microseconds, where ultrafast plasma dynamics are tightly linked to permanent

structural and optical modifications via a unified carrier–stress coupling mechanism (See details in Supplementary Note 6). When femtosecond laser pulses are tightly focused inside transparent fluoride glasses, a cascade of ultrafast electronic and structural transformations is sequentially induced: charge carrier generation occurs on the femtosecond-to-picosecond timescale, specifically via multiphoton and avalanche ionization that forms a dense plasma of free electrons and holes. For fluoroindate (INF) glass, time-resolved pump–probe imaging confirms a linear correlation between plasma electron density and pulse energy, reaching a saturation threshold at 0.8 μJ and generating a transient plasma with an electron density of 4.73×10^{20} cm^{-3} (at a 1.2 ps time delay). Energy deposited in the plasma is transferred to the lattice via electron–phonon coupling, inducing localized rapid heating and thermal expansion—driving stress wave generation (picosecond-to-nanosecond timescale) and temperature gradient formation. This energy transfer efficiency increases with free electron concentration, as higher electron densities enhance electron–phonon collision frequencies, accelerating the conversion of electronic kinetic energy to lattice thermal energy. Birefringence imaging captures radial stress wave propagation at ~ 4.3 μm/ns, with maximum stresses of ~ 1.47 GPa (100 ps) at the femtosecond focal center and ~ 1.23 GPa (800 ps) at the stress wave periphery—corresponding to local temperature rises (ΔT) of ~ 1500 K and ~ 1250 K, respectively. These results reflect the conversion of mechanical energy to thermal energy within the lattice.

Gigapascal-level thermoelastic pressure generated at the femtosecond pulse focal region propagates as longitudinal acoustic waves through the glass matrix. The resulting thermal and pressure gradients drive directional elemental migration: wavelength dispersive spectrometer (WDS) and Raman spectroscopy results reveal that high-polarizability heavy metal cations (Pb^{2+}, In^{3+}) are enriched in the densified high-pressure central zone, while thermal diffusion displaces light anions (F^-) and Ba^{2+} toward the peripheral rarefied regions. This migration maintains local charge neutrality, a behavior consistently observed in ABYPM glass. Elemental redistribution modulates the refractive index (Δn) via changes in local polarizability, ultimately yielding a refractive index contrast of 10^{-2} in fluoroindate glass. Leveraging these insights, we fabricated channel-type optical waveguides in INF glass via multi-scan writing, achieving a minimum insertion loss of ~ 0.7 dB/cm. Heat treatment near the glass transition temperature partially erases femtosecond-modified regions (under low pulse energies). Additionally, vertical translation-based repetitive writing enables mutual conversion of positive and negative Δn regions, providing a flexible strategy for waveguide structure design.These results establish a quantitative framework that bridges ultrafast plasma dynamics and permanent structural modification, offering a unified understanding of femtosecond laser–glass interaction across diverse material systems.

In summary, we reveal the multiscale physical mechanisms that bridge femtosecond laser energy deposition and permanent structural modification in fluoride glasses. Through time-resolved plasma and stress diagnostics combined with microscopic analyses, we demonstrate that nonlinear ionization, stress wave propagation, and ion-selective migration collectively define the nature and sign of refractive index changes. The observed gigapascal-level stresses and compositionally induced polarizability

gradients provide direct evidence that femtosecond laser modification is governed by a coupled plasma–stress–migration process rather than purely thermal relaxation. This mechanistic understanding offers predictive control over refractive index contrast and waveguide morphology, enabling the design of high-performance fluoride glass devices for mid-infrared integrated photonics. Beyond a single material system, the revealed structure–property correlations establish a general framework for understanding ultrafast laser–matter interaction in glasses, guiding the next generation of laser-written photonic architectures and hybrid glass-based platforms.

Materials and methods

Femtosecond laser time-resolved pump-probe shadowgraphy

A femtosecond laser time-resolved pump-probe imaging system was constructed using a Spectra Physics Spirit HE 1040-30-SHG laser to detect plasma and stress wave phenomena induced in fluoride glasses by femtosecond laser irradiation. The laser operates at a central wavelength of 1040 nm, with a pulse duration of 400 fs and a Gaussian spatial beam profile. The repetition rate was set to 10 Hz, enabling detection processes to complete within 0.1 s. The laser beam was split by a beam splitter (BS) into pump and probe beams. In the pump path, power was adjusted via a variable attenuator (At), and a half-wave plate (HWP) rotated the pump beam to vertical polarization to avoid interference with the probe beam; a light shutter (LS) controlled pump beam on/off. The pump beam was then focused onto the side of the glass sample using a microscope objective (20×, NA = 0.4, Mitutoyo M Plan Apo NIR), yielding a focal spot diameter of ~ 2.1 μm. For the probe beam, after splitting, it passed through a delay stage consisting of two mirrors (M3, M4) mounted on a computer-controlled one-dimensional translation stage, allowing precise optical path adjustment for accurate time delays. The probe beam was frequency-doubled to 520 nm (green light) via a β-barium borate (BBO) crystal; after filtering out the fundamental wavelength, it propagated perpendicularly to the pump direction through the sample and was collected by a second microscope objective. Femtosecond laser-induced plasma transmission shadow images were recorded on a charge-coupled device (CCD). The glass sample was fixed on a three-dimensional translation stage for precise control of the laser focal position inside the sample. The CCD, femtosecond laser, and optical shutter were synchronized via electrical signals to ensure one image per pump pulse. The system’s time resolution is determined by the laser pulse duration, with a delay range (from hundreds of femtoseconds to several nanoseconds) defined by the optical delay line. Sequential imaging at different probe delays enables visualization of laser-induced plasma evolution, with time-resolved contrast arising from electron plasma absorption of the probe beam and related phenomena.

The transient stress detection system is modified from the femtosecond pump-probe system. The pump beam, after beam expansion, is reflected into an objective lens via a dichroic mirror (1040 nm HR, 520 nm HT) and focused inside the sample to induce stress waves. The probe beam first passes through a

short-pass filter (SPF), then a linear polarizer (LP), and a quarter-wave plate (optical axis at 45° to the horizontal) to convert it to circularly polarized light. It then propagates through the sample in the opposite direction to the pump beam; the pump-induced internal stress in the sample generates a transient birefringence effect, which modifies the polarization state of the probe beam as it traverses the laser-irradiated region of the glass. Subsequently, the probe beam is focused via an objective lens onto a polarization camera (P-CCD) to capture images of polarized transmitted light. The P-CCD employs a pixel-level polarizer array for spatial modulation, consisting of 2×2 linear polarizer units (0°, 45°, 135°, 90°) forming a pixel array. Polarization information for each direction is extracted from the array, enabling synchronous acquisition of all four polarization states in a single shot.

Fabrication of fluoride glass

Plasma and stress wave detection, alongside femtosecond laser writing of optical waveguides, were demonstrated using home-made fluoride glass materials with distinct matrix compositions. Fluoride glass synthesis was achieved via the melt-quenching method, with the protocol detailed herein using fluoroindate (INF) glass as a representative example. The composition of fluoroindate glass was as follows: $29InF_3 - 16ZnF_2 - 15BaF_2 - 11GaF_3 - 6SrF_2 - 12PbF_2 - 5LiF - 2YF_3 - 2LaF_3 - 2NaF$. For synthesis, 20 g of high-purity (99.99%) fluoride powders were weighed in a nitrogen-filled glove box, mixed with 20% ammonium hydrogen fluoride, and ground thoroughly in an agate mortar. The mixture was transferred to a platinum crucible and fluorinated at 400^{o}C for 30 min in a muffle furnace. After cooling, an additional 20% ammonium hydrogen fluoride was added, followed by re-grinding; the mixture was then placed back into the platinum crucible and melted at 950^{o}C for 3 h in a nitrogen-purged muffle furnace (housed in the glove box). The molten glass was cast into a preheated brass mold and annealed at 230^{o}C for 5 h to eliminate internal stress. Finally, the glass was polished and cut into 10×10×2 mm specimens for subsequent characterization. Other fluoride glasses discussed in this study—including fluoroaluminate (ABYPM) and fluorozincate (AZF, AZFD) glasses—were fabricated via the same protocol as fluoroindate glasses, with the only difference being the annealing temperature (See details of the fluoride glass fabrication parameters in Supplementary Note 7).

Material analysis and characterizations

Transmittance spectra were acquired using a PerkinElmer LAMBDA 750 UV-visible-near-infrared (UV-Vis-NIR) spectrophotometer and a PerkinElmer Fourier-transform infrared (FT-IR) spectrometer. Refractive indices were measured with a SENTECH SER850 ellipsometer over the range of 200–1700 nm. Thermal characteristic curves were obtained via a NETZSCH STA 449 differential thermal analyzer (DTA) between 100°C and 450°C. Backscattered images and elemental distribution maps of the waveguide region were collected using a JEOL (JXA-8230) electron probe microanalyzer (EPMA).

Declarations

Competing interests

The authors declare no competing interests.

Author contributions

P.W. conceived the idea and supervised the research. L.M. performed fluoride glass fabrication, waveguide writing, optical measurements, EPMA characterizations, and Raman spectroscopy under the supervision of P.W. and S.J. J.W. and J.D. conducted plasma and stress wave detection and theoretical calculations under the guidance of X.L. and S.Z. C.L. prepared glass samples for EPMA testing with assistance from S.W. L.S conducted theoretical simulations under the guidance of P.W. All authors analyzed the results and contributed to the manuscript, which was initially drafted by L.M. and J.W.

Acknowledgements

We thank Professor Sujuan Huang and Ning Ma (Shanghai University) for measuring the refractive index distribution across the cross-section of femtosecond laser direct writing optical waveguides. This work was supported by the National Key Research and Development Program of China (2020YFA0607602, 2021YFB3500901), the National Natural Science Foundation of China (NSCF) (62090062, 62105079, 62225502, 62225507, 62375061), the Fundamental Research Funds for the Central Universities (3072025WD2501), the CAS Project for Young Scientists in Basic Research (YSBR-065).

Data availability

The data that support the findings of this study are available from the corresponding authors on reasonable request.

References

1. M. R. Majewski, R. I. Woodward & S. D. Jackson. Dysprosium-doped ZBLAN fiber laser tunable from 2.8 μm to 3.4 μm, pumped at 1.7 μm. *Opt. Lett.* **43**, 971-974 (2018).
2. J. Zhang, M. Liu, J. Yu, R. Wang, S. Jia, Z. Liu, G. Farrell, S. Wang & P. Wang. Praseodymium mid-infrared emission in AlF_3-based glass sensitized by ytterbium. *Opt. Express* **29**, 34166-34174 (2021).
3. S. D. Jackson. Towards high-power mid-infrared emission from a fibre laser. *Nat. Photonics* **6**, 423-431 (2012).
4. J. Wang, S. Wang, X. Zhou, M. Liu, H. Wu, Y. Yin, Z. Qin, G. Xie, Z. Li, P. Wang & Y. Liu. Generation of tunable Raman soliton and dispersive wave beyond 4 μm in centimeter-length fluorotellurite fibers. *Light*:*Sci. Appl.* **14**, 340 (2025).
5. Y. O. Aydin, V. Fortin, R. Vallée & M. Bernier. Towards power scaling of 2.8 μm fiber lasers. *Opt. Lett.* **43**, 4542-4545 (2018).

6. G. Ishida, M. Sugimoto, H. Uehara, S. Tokita, Y. Nishijima & K. Goya. Fiber-in-line infrared spectrometer fabricated by femtosecond laser structuring of microchannels in fluoride glass fiber. *Opt. Express* **33**, 35550-35559 (2025).
7. L. Zhang, Y. Sun, Y. Jiang, B. Da, J. Du, S. Wang, S. Qi, Z. Yang, L. Zhang & J. He. Transparent fluoride glass-ceramics with phase-selective crystallization for middle IR photonics. *J. Mater. Chem. C* **10**, 12947-12956 (2022).
8. L. Zhang, S. Fu, Q. Sheng, X. Luo, J. Zhang, W. Shi & J. Yao. Pump quantum efficiency optimization of 3.5 μm Er-doped ZBLAN fiber laser for high-power operation. *Front. Optoelectron.* **16**, 33 (2023).
9. R. R. Gattass & E. Mazur. Femtosecond laser micromachining in transparent materials. *Nat. Photonics* **2**, 219-225 (2008).
10. K. Sugioka & Y. Cheng. Ultrafast lasers—reliable tools for advanced materials processing. *Light*:*Sci. Appl.* **3**, e149-e149 (2014).
11. B. C. Stuart, M. D. Feit, S. Herman, A. M. Rubenchik, B. W. Shore & M. D. Perry. Nanosecond-to-femtosecond laser-induced breakdown in dielectrics. *Phys. Rev. B* **53**, 1749-1761 (1996).
12. T. T. Fernandez, B. Johnston, H. Mahmodi, K. Privat, I. Kabakova, S. Gross, M. Withford & A. Fuerbach. Thermally stable high numerical aperture integrated waveguides and couplers for the 3 μm wavelength range. *APL Photonics* **7**, 126106 (2022).
13. L. M. Marcondes, J. R. Orives, L. K. Nolasco, S. N. C. Santos, C. R. Mendonça, T. Cardinal, Y. Petit, L. Canioni, M. Dussauze & M. Nalin. 3D luminescent waveguides micromachining by femtosecond laser inscription in niobium germanate glass. *Opt. Mater.* **159**, 116562 (2025).
14. Z. Zhang, Z. Cheng, S. Wang, C. Guan, S. Jia & P. Wang. Fabrication of double-cladding fluoroindate glass fibers and watt-level 2.7 μm laser application. *Infrared Phys. Technol.* **139**, 105299 (2024).
15. S. Li, Y. Yang, Y. Song, R. Wan, Y. Ma, B. Peng, G. Zhang & P. Wang. Laser-induced fluorescence and its effect on the damage resistance of fluoride-containing phosphate-based glasses. *Ceram. Int.* **47**, 13164-13172 (2021).
16. T. T. Fernandez, Y. Hwang, H. Mahmodi, D. E. Otten, L. Plenecassagne, S. Cozic, S. Gross, I. Kabakova, M. Withford, M. Poulain, A. Fuerbach & D. G. Lancaster. Ultrafast laser-fabricated fluoride glass waveguides with exceptionally high positive refractive index change for mid-infrared integrated optics. *Opt. Express* **32**, 42938-42950 (2024).
17. F. Flamini, L. Magrini, A. S. Rab, N. Spagnolo, V. D'Ambrosio, P. Mataloni, F. Sciarrino, T. Zandrini, A. Crespi, R. Ramponi & R. Osellame. Thermally reconfigurable quantum photonic circuits at telecom wavelength by femtosecond laser micromachining. *Light:Sci. Appl.* **4**, e354-e354 (2015).
18. F. Huang, J. Si, T. Chen, T. Shen, M. Shi & X. Hou. Temporal-spatial dynamics of electronic plasma in femtosecond laser induced damage. *Opt. Express* **29**, 14658-14667 (2021).
19. O. Koritsoglou, G. Duchateau, O. Utéza & A. Mouskeftaras. Quantitative assessment of femtosecond laser-induced stress waves in fused silica. *Phys. Rev. B* **110**, 054112 (2024).
20. R. Beuton, B. Chimier, J. Breil, D. Hébert, K. Mishchik, J. Lopez, P. H. Maire & G. Duchateau. Thermo-elasto-plastic simulations of femtosecond laser-induced multiple-cavity in fused silica. *Appl. Phys. A*

124, 324 (2018).

21. M. Sakakura, M. Terazima, Y. Shimotsuma, K. Miura & K. Hirao. Observation of pressure wave generated by focusing a femtosecond laser pulse inside a glass. *Opt. Express* **15**, 5674-5686 (2007).
22. Y. Liu, M. Shimizu, X. Wang, B. Zhu, M. Sakakura, Y. Shimotsuma, J. Qiu, K. Miura & K. Hirao. Confocal Raman imaging of femtosecond laser induced microstructures in germanate glasses. *Chem. Phys. Lett.* **477**, 122-125 (2009).
23. J. Martínez, A. Ródenas, T. Fernandez, J. R. Vázquez de Aldana, R. R. Thomson, M. Aguiló, A. K. Kar, J. Solis & F. Díaz. 3D laser-written silica glass step-index high-contrast waveguides for the 3.5 μm mid-infrared range. *Opt. Lett.* **40**, 5818-5821 (2015).
24. R. Beuton, B. Chimier, J. Breil, D. Hébert, P.-H. Maire & G. Duchateau. Thermo-elasto-plastic simulations of femtosecond laser-induced structural modifications: Application to cavity formation in fused silica. *J. Appl. Phys.* **122**, 203104 (2017).
25. Y. Wang, L. Zhong, K. Y. Lau, X. Han, Y. Yang, J. Hu, S. Firstov, Z. Chen, Z. Ma, L. Tong, K. S. Chiang, D. Tan & J. Qiu. Precise mode control of laser-written waveguides for broadband, low-dispersion 3D integrated optics. *Light:Sci. Appl.* **13**, 130 (2024).
26. R. P. de Melo, Jr., B. J. P. da Silva, E. L. Falcão-Filho, E. F. da Silva, Jr., D. V. Petrov, C. B. de Araújo, Y. Messaddeq & M. A. Aegerter. Novel fabrication process of planar waveguides in rare-earth doped fluoroindate glasses. *Appl. Phys. Lett.* **67**, 886-887 (1995).
27. K. Miura, J. Qiu, T. Mitsuyu & K. Hirao. Preparation and optical properties of fluoride glass waveguides induced by laser pulses. *J. Non-Cryst. Solids* **256-257**, 212-219 (1999).
28. L. Talbot & M. Bernier. Femtosecond writing of intra-phase-mask volume Bragg gratings. *Opt. Lett.* **48**, 1954-1957 (2023).
29. F. Elan, M. Olivero, E. L. Falcão-Filho, C. B. de Araújo, Y. Messaddeq & A. S. L. Gomes. Femtosecond laser-written waveguides in thulium-doped fluoroindate glass for S-band amplification. *Electron. Lett.* **50**, 540-542 (2014).
30. L. Jiang, A.-D. Wang, B. Li, T.-H. Cui & Y.-F. Lu. Electrons dynamics control by shaping femtosecond laser pulses in micro/nanofabrication: modeling, method, measurement and application. *Light:Sci. Appl.* **7**, 17134-17134 (2018).
31. B. Guo, J. Sun, Y. Lu & L. Jiang. Ultrafast dynamics observation during femtosecond laser-material interaction. *Int. J. Extreme Manuf.* **1**, 032004 (2019).
32. M. Liu, J. Zhang, N. Xu, X. Tian, S. Jia, S. Wang, G. Brambilla & P. Wang. Room-temperature watt-level and tunable ~3 μm lasers in Ho^{3+}/Pr^{3+} co-doped AlF_3-based glass fiber. *Opt. Lett.* **46**, 2417-2420 (2021).
33. L. Zhang, Y. Jiang, Z. Wang, F. Guan, Y. Li, X. Yuan & L. Zhang. Performance and structure evolution of fluoindinate glass at high temperatures. *J. Am. Ceram. Soc.* **105**, 2001-2009 (2022).
34. J. Zhang, R. Wang, M. Liu, S. Wang, Z. Zhang, G. Farrell, S. Jia & P. Wang. ZnF_2-modified AlF_3-based fluoride glasses with enhanced mid-infrared 3.5 μm emission. *J. Am. Ceram. Soc.* **105**, 4691-4698

(2022).

35. Z. Zhang, Z. Cheng, R. Wang, S. Wang, G. Farrell, S. Jia & P. Wang. Deactivation effects of Tb^{3+} on Ho^{3+} emission in fluoroindate glasses for 3.9 μm laser applications. *Ceram. Int.* **49**, 12772-12778 (2023).
36. Q. Yu, S. Wang, Y. Fu, L. Tan, C. Gao, C. Lin & S. Kang. Highly Er^{3+} doped chalcogenide glass with enhanced mid-infrared emission and superior mechanical property. *Opt. Express* **32**, 46131-46139 (2024).
37. F. Quéré, S. Guizard & M. Ph. Time-resolved study of laser-induced breakdown in dielectrics. *Europhys. Lett.* **56**, 138 (2001).
38. D. Du, X. Liu, G. Korn, J. Squier & G. Mourou. Laser-induced breakdown by impact ionization in SiO_2 with pulse widths from 7 ns to 150 fs. *Appl. Phys. Lett.* **64**, 3071-3073 (1994).
39. A. Couairon, L. Sudrie, M. Franco, B. Prade & A. Mysyrowicz. Filamentation and damage in fused silica induced by tightly focused femtosecond laser pulses. *Phys. Rev. B* **71**, 125435 (2005).
40. J. Zhu, Z. Li, T. Liu, Y. Zhu, G. Tang & C. Bai. EXAFS study of $20GaF_3$–$15InF_3$–$20CdF_2$–$15ZnF_2$–$20PbF_2$–$10SnF_2$ glass. *J. Non-Cryst. Solids* **354**, 1182-1184 (2008).
41. S. G. Bakhvalov, E. M. Petrova, A. I. Livshits, A. A. Shubin, V. M. Buznik & V. M. Denisov. IR and NMR studies of the structure of glasses based on gallium and indium trifluorides. *J. Struct. Chem.* **39**, 651-659 (1998).
42. T. N. Vasudevan & R. S. Krishnan. Dispersion of the stress-optic coefficient in glasses. **5**, (1972).
43. M. Sakakura. Observation of Stress Wave and Thermal Stress in Ultrashort Pulse Laser Bulk Processing inside Glass. **12**, 164 (2017).
44. N. Ma, C. Yan & S. Huang. 2D refractive index measurement for direct laser writing waveguides with complex structures. *Opt. Express* **33**, 16210-16221 (2025).
45. L. Mao, T. Gong, Z. Zhao, S. Jia, S. Wang & P. Wang. Low-Loss Optical Channel Waveguides in ZnF_2-AlF_3 Based Fluoride Glass for Integrated Photonics. *IEEE Photonics Technol. Lett.* **37**, 1405-1408 (2025).
46. J.-P. Bérubé, M. Bernier & R. Vallée. Femtosecond laser-induced refractive index modifications in fluoride glass. *Opt. Mater. Express* **3**, 598-611 (2013).
47. O. Dematteo Caulier, K. Mishchik, B. Chimier, S. Skupin, A. Bourgeade, C. Javaux Léger, R. Kling, C. Hönninger, J. Lopez, V. Tikhonchuk & G. Duchateau. Femtosecond laser pulse train interaction with dielectric materials. *Appl. Phys. Lett.* **107**, 181110 (2015).
48. T. T. Fernandez, B. Johnston, S. Gross, S. Cozic, M. Poulain, H. Mahmodi, I. Kabakova, M. Withford & A. Fuerbach. Ultrafast laser inscribed waveguides in tailored fluoride glasses: an enabling technology for mid-infrared integrated photonics devices. *Sci. Rep.* **12**, 14674 (2022).

Figures

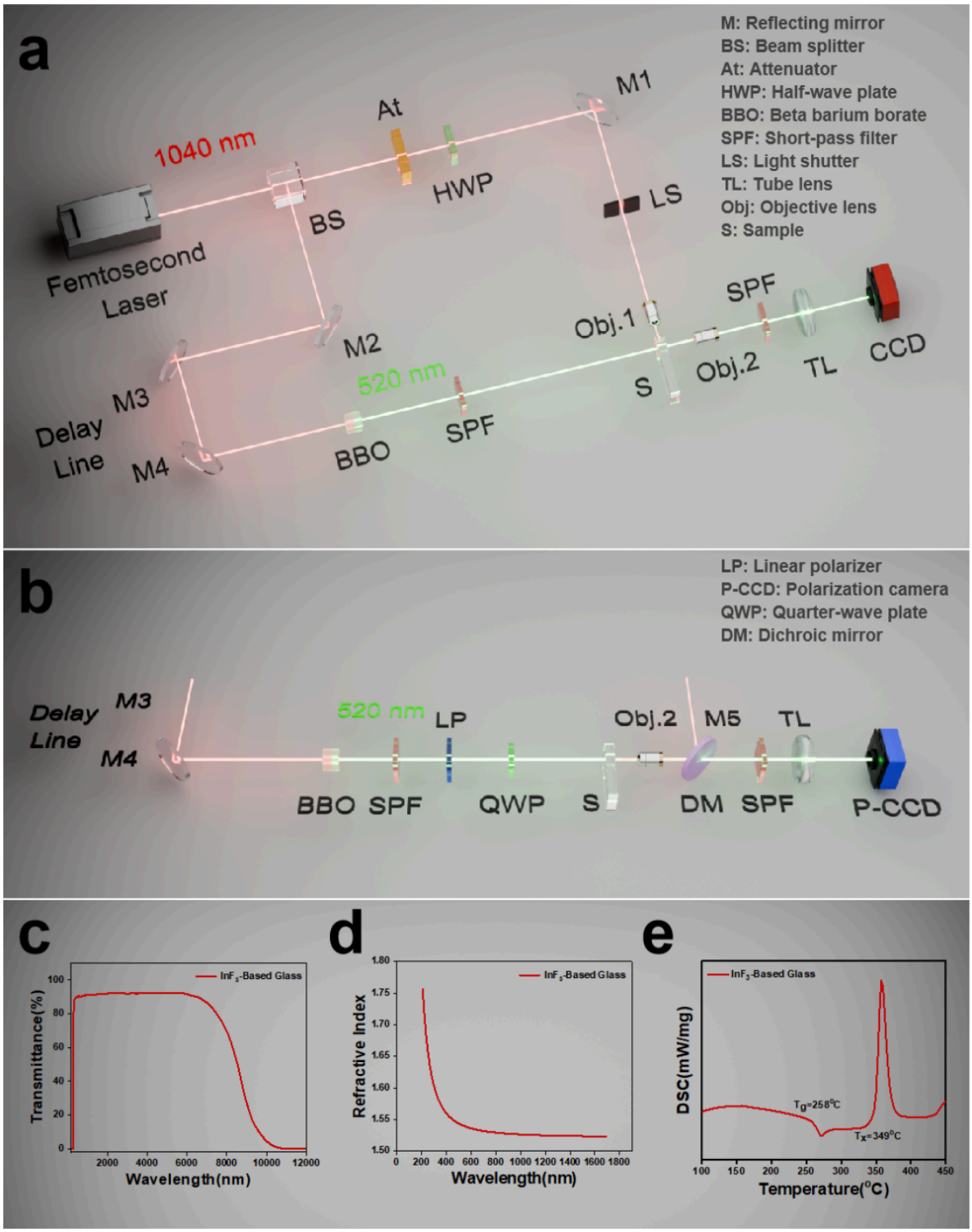


Figure 1

Schematic of pump-probe shadowgraphy systems and material properties of fluoroindate glass. a Schematic of the time-resolved pump-probe shadowgraphy system for detecting femtosecond laser-induced plasma in glass. **b** Schematic of the improved birefringence imaging system for stress wave characterization. **c**Transmittance spectrum of fluoroindate glass (200 nm–12 μm). **d**Refractive index

profile of fluoroindate glass (200 nm–1700 nm). **e**Differential thermal analysis curve of fluoroindate glass (100–450°C).

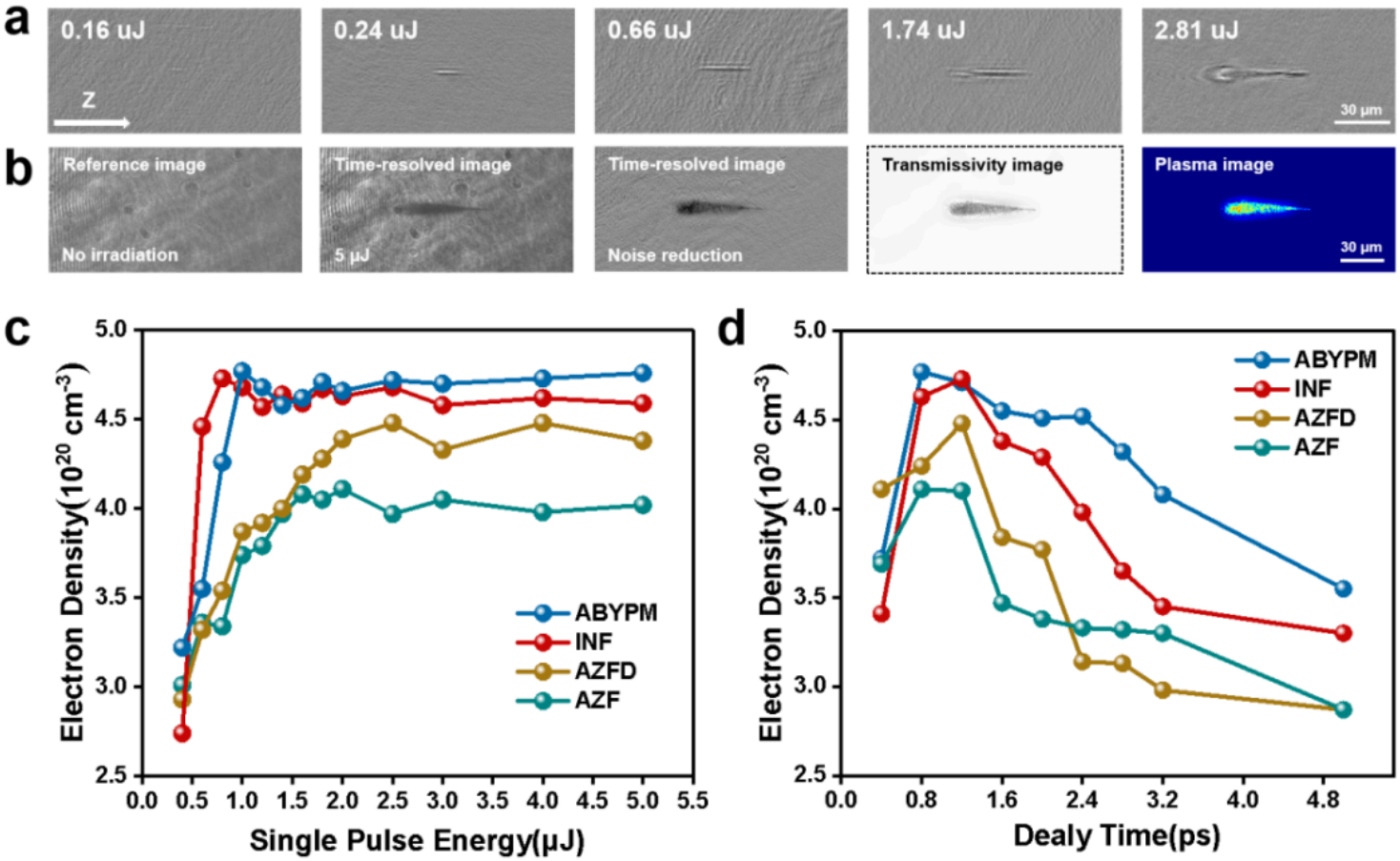


Figure 2

Femtosecond laser-induced plasma phenomena in fluoride glasses. a CCD-captured images of femtosecond laser-induced electron plasma under different single-pulse energies. The femtosecond laser is incident along the Z-direction, with a modification depth of 160 μm; weak plasma is observed at 0.16 μJ. **b**Reference image (before femtosecond laser incidence), time-resolved image (800 fs, single-pulse energy: 5 μJ), denoised image, corresponding transmittance image, and simulated plasma image. **c** Electron density evolution of different fluoride glass materials under varying single-pulse energies (0.4-5 μJ). **d** Spatiotemporal evolution of different fluoride glass materials at saturated electron density (INF: 0.8 μJ; ABYPM: 1 μJ; AZF: 2 μJ; AZFD: 2.5 μJ).

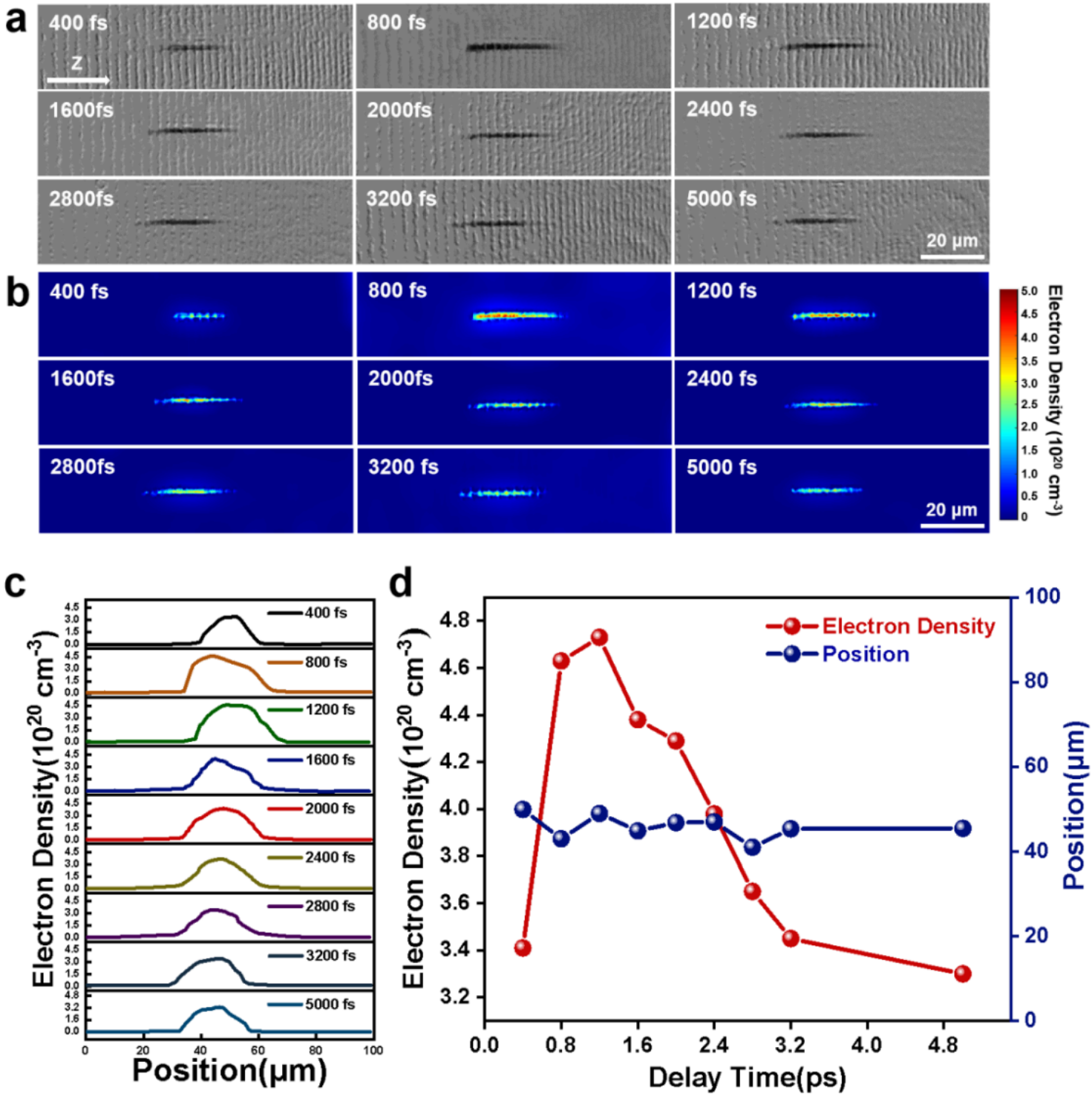


Figure 3

Time-resolved plasma images and electron density of INF glass under 0.8 μJ. a Temporal-spatial evolution images of femtosecond laser-induced plasma at different time delays (400 fs–5 ps). The femtosecond laser is incident along the Z-direction, with a modification depth of 160 μm from the glass surface. **b**Temporal-spatial evolution image of electron density. For clarity, the leftmost boundary of the image is defined as the 0 μm position, corresponding to 115 μm below the glass surface. **c** Spatial

distributions of transient electron density along the plasma axis at different delay times. **d**Temporal-spatial evolution of the transient peak electron density.

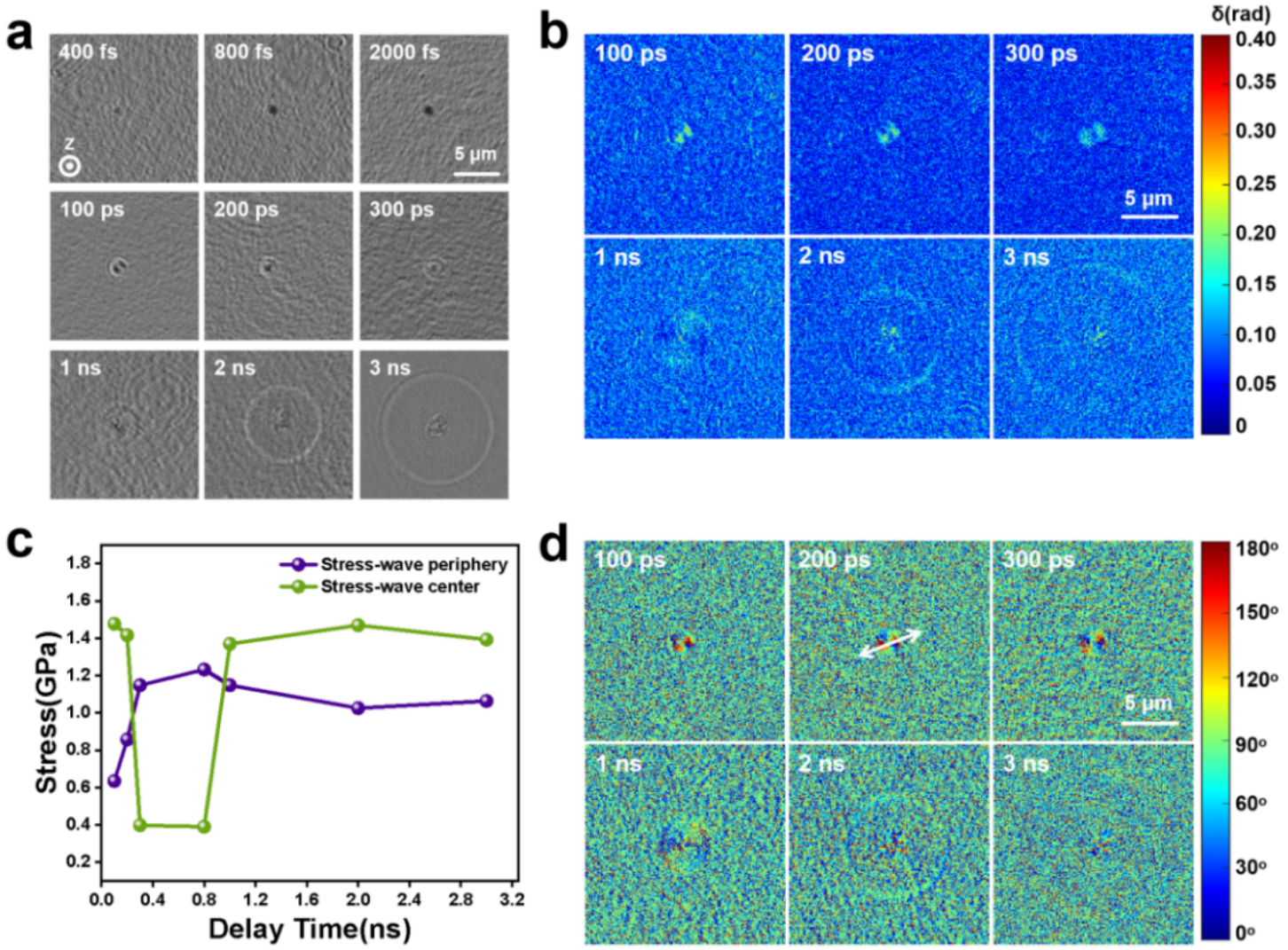


Figure 4

Time-resolved stress wave images of INF glass under 0.8 μJ. a Dynamic optical transmission images at different time delays (400 fs–3 ns). The femtosecond laser is perpendicular to the observer along the Z direction while the probe pulse is opposite. **b** Optical retardance images at time delays of 100 ps–3 ns. No optical retardance is observed before 100 ps. **c** Distribution of stress difference with pump-probe time delay, covering the central and peripheral regions of stress waves. **d** Slow axis of birefringence distribution images at time delays of 100 ps–3 ns.

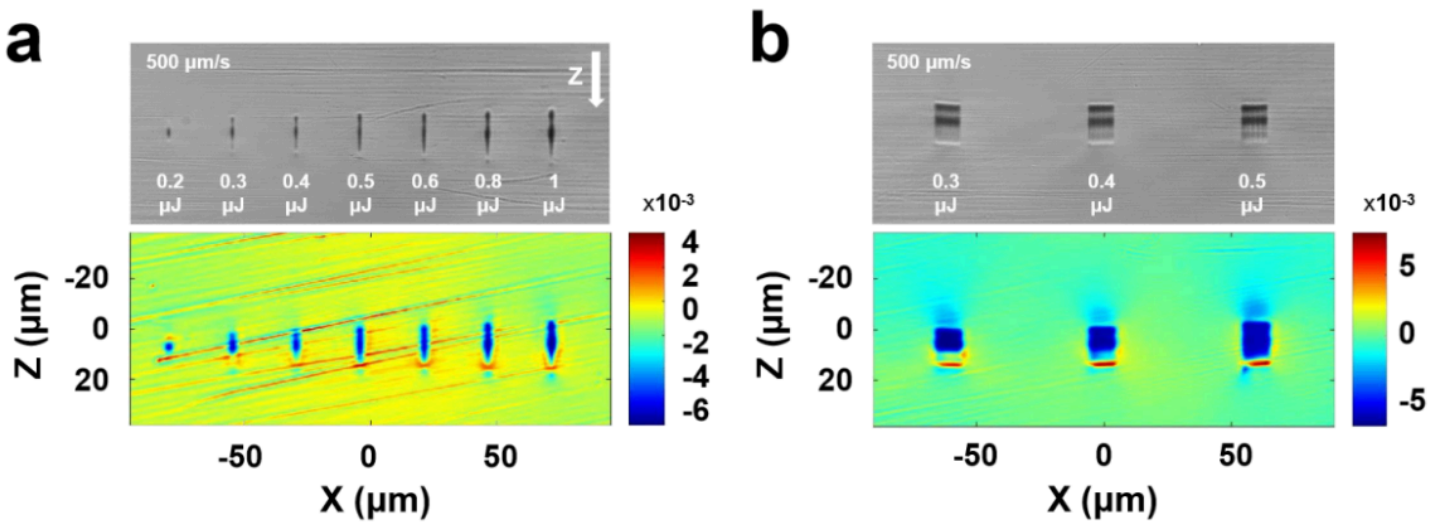


Figure 5

Refractive index distribution and Raman spectrum of femtosecond laser-modified region under 1 kHz repetition rate. a Refractive index distribution of the cross-section in single-line written regions under different single-pulse energies. **b** Refractive index distribution of the cross-section in channel-type waveguides under different single-pulse energies.

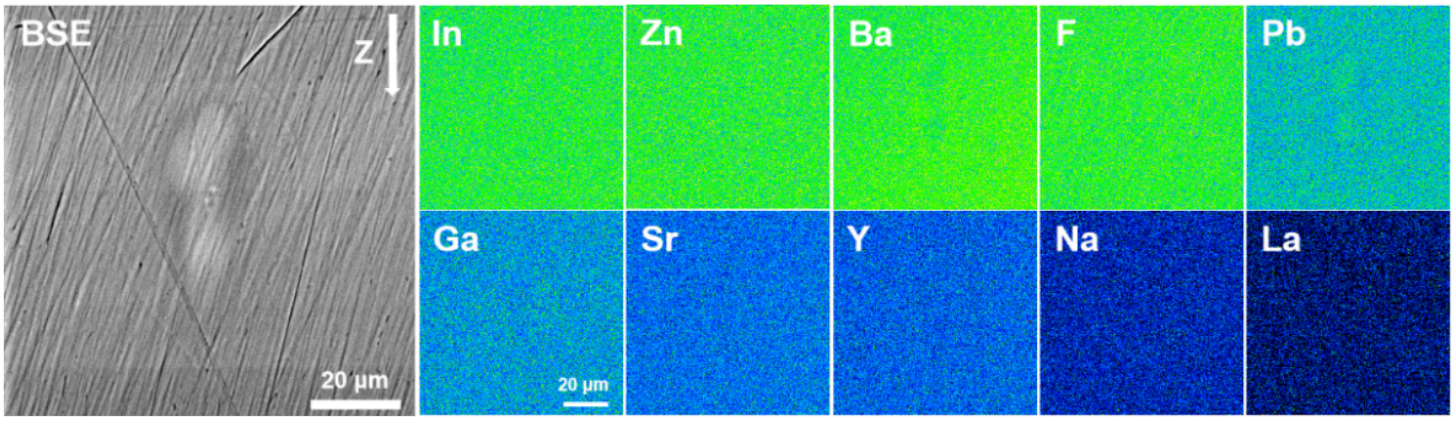


Figure 6

Elemental distribution in the cross-section of femtosecond laser-modified regions (INF glass). Backscattered electron (BSE) image and corresponding elemental distribution maps (from electron probe microanalysis). This region was fabricated via single-line scanning with a femtosecond laser (repetition rate: 50 kHz; scanning speed: 500 μm/s; single-pulse energy: 3 μJ).

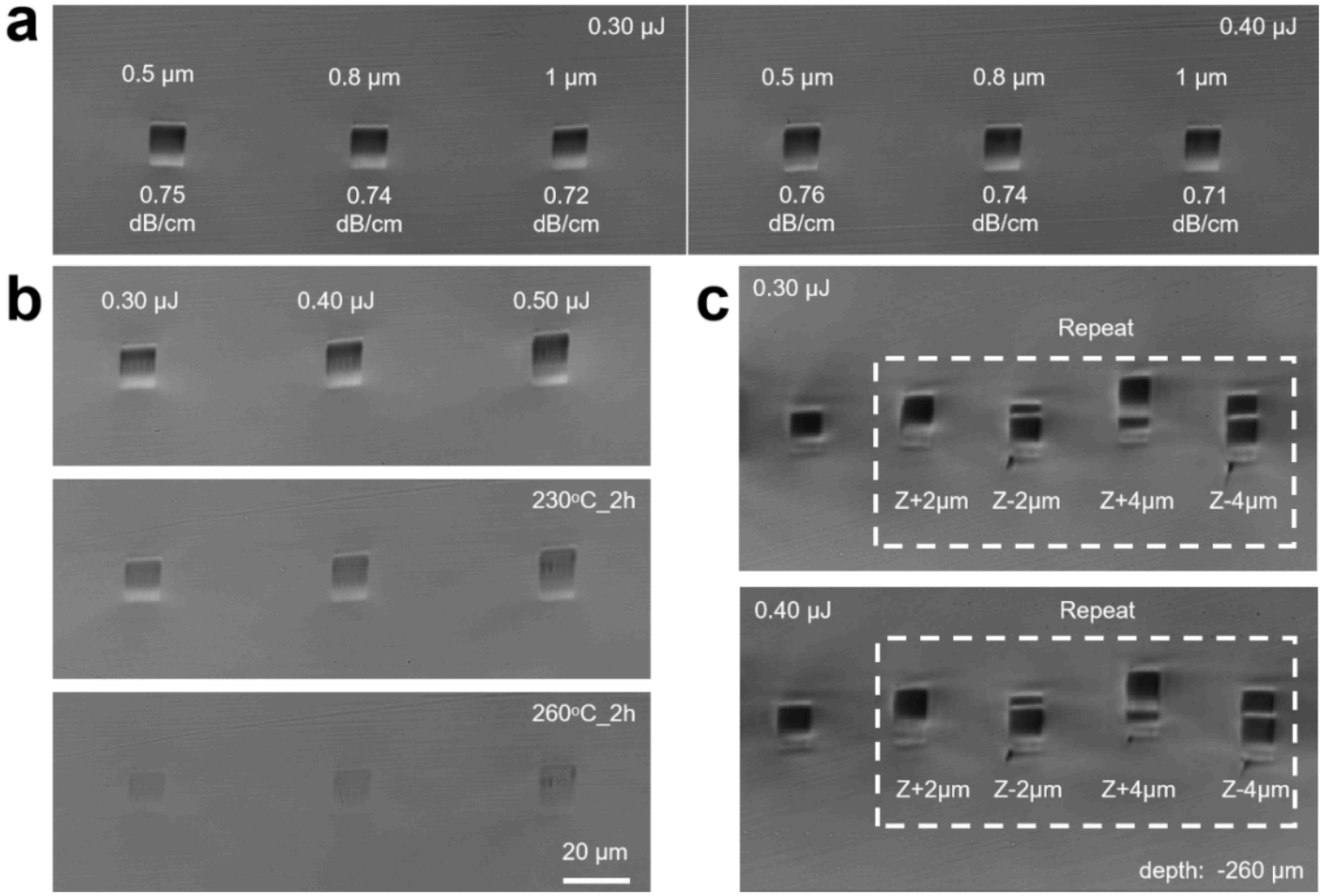


Figure 7

General characteristics of channel waveguides in INF glass. a Femtosecond direct-writing channel optical waveguides fabricated with different single-pulse energies (0.3 μJ, 0.4 μJ) and writing intervals (0.5–1 μm). **b**Thermal erasure of optical waveguides under different heat-treatment temperatures. **c** Vertical translation repetitive writing method for high proportion construction of positive refractive index modified regions (e.g., 'z+2 μm' denotes 2 μm downward translation of the glass sample relative to the femtosecond laser incidence direction).

Supplementary Files

This is a list of supplementary files associated with this preprint. Click to download.

- Supplementaryinformation.docx
- Video2RealtimeObservationofFemtosecondLaserdrivenStressWavesinFluorideGlass.mp4
- Video1RealtimeObservationofFemtosecondLaserinducedPlasmaDynamicsinFluorideGlass.mp4